Directing charge transfer in a chemical-bonded Ni/Cd$_{0.7}$Mn$_{0.3}$S Schottky heterojunction for selective photocatalytic oxidation of benzyl alcohol structural organic platform molecules coupled with hydrogen evolution reaction

Hua Wen [a,1], Wen Duan [a,1], Li Guo [a], Qi Wang [a], Xin Fu [a], Yuhui Wang [a], Ruqi Li [a], Binbin Jin [b], Rui Du [a], Chunming Yang [a], Danjun Wang [a,*]

[a] College of Chemistry & Chemical Engineering, Yan'an University, Shaanxi Key Laboratory of Chemical Reaction Engineering, Yan'an 716000, PR China
[b] Chongqing Key Laboratory of Inorganic Special Functional Materials, College of Chemistry and Chemical Engineering, Yangtze Normal University, Chongqing 408100, PR China

ARTICLE INFO

ABSTRACT

Solar-energy-driven half-reactions coupling is a vital photocatalysis strategy to simultaneously realize low-value organic platform molecules value-added conversion and hydrogen production. It is essential to design photocatalyst with appropriate band structures and efficient spatial separation of photogenerated hole/electron pairs (h$^+$/e$^-$) to drive reduction/oxidation half-reactions, respectively. Herein, chemical-bonded Ni/Cd$_{0.7}$Mn$_{0.3}$S Schottky junction was constructed via hydrothermal-chemical reduction method for sunlight-driven catalytic selective dehydrogenation oxidization of benzyl alcohol (BA) coupling with hydrogen evolution reaction (HER). The optimal 8% Ni/Cd$_{0.7}$Mn$_{0.3}$S exhibited excellent BA conversion rate (77%), benzaldehyde (BAD) yield (2.88 mmol·g^{-1}·h^{-1}), selectivity (99%) and HER activity (2.94 mmol·g^{-1}·h^{-1}). The selective oxidation of BA and its para-substituents (-CH$_3$, -OCH$_3$, -Br, -NO$_2$) proceeded a carbon-centred radical mechanism via the cleavage of α_{C-H} bond. Furthermore, the Ni/Cd$_{0.7}$Mn$_{0.3}$S exhibits excellent selective oxidation of the other organic platform molecules with benzyl alcohol structure, such as 5-hydroxymethylfurfural (HMF) and vanillyl alcohol (VAL), *etc*, validating that the chemical-bonded Ni/Cd$_{0.7}$Mn$_{0.3}$S possess the excellent performance in α_{C-H} bond activation of benzyl alcohol structure unit. By combining experiment and DFT calculation results, the Ni-S bond formed at Ni/Cd$_{0.7}$Mn$_{0.3}$S interface can accelerate the directing charge transfer, thus boosting the organic platform molecules selective oxidation coupling with HER.

1. Introduction

In the face of the exacerbation of environmental issue and the lack of fossil fuel, hydrogen (H$_2$) as a high energy density, non-polluted, storable and renewable energy source, is an ideal alternative energy to resolve the current environmental pollution problem and energy crisis [1–4]. Nowadays, solar-energy-driven photocatalytic hydrogen evolution reaction (HER) through water splitting is regarded as a significant technology for generating clean hydrogen energy, which can effectively convert solar energy into chemical energy [5]. Unfortunately, the kinetic-sluggish water oxygen evolution reaction (OER) require the use

of hole trapping agent (e.g., methanol, ethanol, lactic acid, Na$_2$S/-Na$_2$SO$_3$, *etc*.) to capture the photogenerated holes, thus facilitating the photocatalytic HER. However, sacrifice agent can be oxidized to useless by-product even produce carbon emission. Consequently, it is promising to use low-value organic platform molecules instead of sacrificial agents, simultaneously achieving highly efficient HER and selective dehydrogenation oxidation of organic platform molecules to value-added chemicals [6–11].

Transition metal sulfides (TMSs) are considered as the ideal photocatalytic material for their inherent character of narrow bandgap for light harvesting capacity and low-work function, especially CdS [12,13].

Nevertheless, CdS still faces issues of rapid recombination of photo-generated charge/hole and photo-corrosion [14]. So far, researchers have developed a large number of multi component sulfide solid solutions with adjustable band gap for photocatalysis HER [15]. $Cd_{1-x}Mn_xS$ is one of the n-type sulfide solid solutions semiconductor with band gap (2.1–2.4 eV) and higher stability than that of CdS [16,17]. Nevertheless, the pristine $Cd_{1-x}Mn_xS$ still suffer from the barrier of low charge carriers separation efficiency [18,19]. Therefore, it is vital to promote the separation/transfer of photogenerated carriers on the $Cd_{1-x}Mn_xS$ [20]. To this end, many methods have been employed, such as constructing hetero-structure by loading co-catalyst [21]. Until now, noble metals have generally been used as efficient co-catalysts to boost surface reaction, while the rareness and expensiveness limited its large-scale use [22–24]. Transition metal Ni was a conventional hydrogenation/dehydrogenation catalyst owing its cheapness and unique *d*-electronic configuration ($3d^8$). It was usually employed as co-catalyst for the formation of Schottky junctions to promote the separation/-transfer of photogenerated carriers [25,26]. Accordingly, Ni loading on the surface of $Cd_{1-x}Mn_xS$ is expected to further drive the spatial separation of photogenerated carriers as well as accelerate its directing transfer [27].

In this paper, chemical-bonded $Ni/Cd_{0.7}Mn_{0.3}S$ Schottky junction was designed and constructed by hydrothermal and chemical reduction method, which selectively photocatalytic oxidation of BA to BAD coupling with HER. The 8% $Ni/Cd_{0.7}Mn_{0.3}S$ exhibits outstanding photocatalytic performance and chemical durability, achieving efficient HER rate (2.94 mmol·g^{-1}·h^{-1}), BAD yields reach 2.88 mmol·g^{-1}·h^{-1} and showed high conversion of BA (77%), while BAD selectivity (99%). The boosted photocatalytic HER activity of $Ni/Cd_{0.7}Mn_{0.3}S$ Schottky junction might be ascribed to the formation of chemical-bonded $Ni/Cd_{0.7}Mn_{0.3}S$ Schottky junction between Ni and $Cd_{0.7}Mn_{0.3}S$, which was benefited to the directing charge transfer at $Ni/Cd_{0.7}Mn_{0.3}S$ interface and accelerate separation/migration of photogenerated carriers. Metallic nickel chemical bonded on $Cd_{0.7}Mn_{0.3}S$ nanorods via the formation Ni-S bond act as admirable electron acceptors and providing a widespread range of active sites for proton (H^+) reduction. By exploring the selective oxidation of benzyl alcohol with different substituents (-CH₃, -OCH₃, -Br, -NO₂), it was found that the electron-donating groups (-CH₃, -OCH₃) could promote the oxidization of BA to BAD. Furthermore, the $Ni/Cd_{0.7}Mn_{0.3}S$ exhibits excellent selective oxidation of 5-hydroxymethylfurfural (HMF) and vanillyl alcohol (VAL), etc, validating that the chemical-bonded $Ni/Cd_{0.7}Mn_{0.3}S$ possess the excellent performance in α_{C-H} bond activation of benzyl alcohol structure unit. This study demonstrated that construction of chemical-bonded Schottky heterojunction is an efficient strategy to boost the photocatalytic HER coupling with low-value organic platform molecules with benzyl alcohol structure to value-added conversion.

2. Experimental section

2.1. Synthesis of $Cd_{1-x}Mn_xS$

The synthesis $Cd_{1-x}Mn_xS$ (CMS) were similar as previous report [28]. Typically, 1.87 g of Cd(CH₃COO)₂·2 H₂O, 0.74 g of Mn (CH₃COO)₂·4 H₂O and 1.13 g of TAA were dispersed in 60 mL EDTA with stirring at room temperature for 1 h. Then, transfer the solution to 80 mL Teflon-lined stainless-steel and maintained at 200 ℃ for 24 h. After the hydrothermal reaction, the yellow precipitates were centrifuged and washed with deionized water and ethanol for three times, and dried in the oven at 60 ℃ overnight. The as-prepared sample was denoted as $Cd_{0.7}Mn_{0.3}S$. Varying the Mn(CH₃COO)₂·4 H₂O while keep the amount of Cd(CH₃COO)₂·2 H₂O and TAA unchanging, a series of $Cd_{1-x}Mn_xS$ solid solution was obtained and denoted $Cd_{1-x}Mn_xS$, while x mean the mole ratio of Mn and Cd element (x = 0.1, 0.3, 0.5, 0.7, 0.9).

2.2. Synthesis of chemical-bonded $Ni/Cd_{0.7}Mn_{0.3}S$

The synthesis x% $Ni/Cd_{0.7}Mn_{0.3}S$ were prepared via an ordinary chemical reduction-deposition, in which Lysine and NaBH₄ were used as capping agent and reducing agent, respectively. Typically, 0.5 g of as-prepared $Cd_{0.7}Mn_{0.3}S$ was scattered in 10 mL deionized water, then 16.8 mL of 0.01 mol·L^{-1} NiCl₂·6 H₂O and 6.0 mL of 0.01 mol·L^{-1} Lysine were added dropwise in 30 min. Thereafter, 5.3 mL of 0.1 mol·L^{-1} NaBH₄ was added during the ultrasound. Afterward, the suspension was centrifugal washed with deionized water for four times and dried at 60 ℃ in vacuum for 12 h. The obtained catalysts were denoted as 8% Ni/$Cd_{0.7}Mn_{0.3}S$. Varying the added content of NiCl₂·6 H₂O, a series of Ni/$Cd_{0.7}Mn_{0.3}S$ was obtained and denoted x% Ni/$Cd_{0.7}Mn_{0.3}S$ (x = 2, 4, 6, 8, 10). x is the mass ratio of NiCl₂·6 H₂O to $Cd_{0.7}Mn_{0.3}S$. In addition, 8% NiS/$Cd_{0.7}Mn_{0.3}S$ was prepared according to our previous reports [47].

For comparison, CdS nanorods were also synthesized through a simple hydrothermal process. Typically, 4.1 g of Cd(CH₃COO)₂·2 H₂O and 1.13 g of TAA were dissolved into 30 mL EDTA, then kept stirring for 1 h at room temperature and then transferred in to a 80 mL PTFE lined stainless-steel autoclave and heated at 190 ℃ for 24 h. Then, the yellow precipitates were centrifuged and washed with water and ethanol, and dried at 60 ℃ overnight. The synthesis of MnS cubes is similar to CdS, except that 4.1 g Cd(CH₃OO)₂·2 H₂O is replaced by 3.7 g Mn (CH₃COO)₂·4 H₂O.

2.3. Photocatalytic activity and selective oxidation of BA to BAD

Photocatalytic oxidation benzyl alcohol (BA) to benzaldehyde (BAD) coupling with hydrogen production experiment were executed in a sealed glass reactor with a closed online gas circulation and evacuation system (Labsobar-IIIAG, Beijing Pect Light Technology Co., Ltd). In a typical reaction, 30 mg of catalysts were ultrasonically dispersed in 100 mL of DI water, containing 50 μL benzyl alcohol. The dark reaction lasted for 1 h and benzyl alcohol was adsorbed on the catalyst, followed by 4 h of light exposure. Before the reaction began, 3 mL of the sample was taken, and after the reaction ended, 3 mL of the sample was filtered and extracted with ethyl acetate. The product was detected using GC 7980 gas chromatography to determine the concentration of benzyl alcohol and benzaldehyde. The conversion of BA and the selectivity of BAD are computed using the as below formula:

$$\textbf{Conversion}(\%) = \frac{\textbf{C}_0 - \textbf{C}_{BA}}{\textbf{C}_0} \times 100\% \tag{1}$$

$$\textbf{Selectivity}(\%) = \frac{\textbf{C}_{BAD}}{\textbf{C}_0 - \textbf{C}_{BA}} \times 100\% \tag{2}$$

3. Results and discussion

3.1. Construction of chemical-bonded $Ni/Cd_{0.7}Mn_{0.3}S$ Schottky junction

Fig. S1 illustrates the fabrication process of $Ni/Cd_{0.7}Mn_{0.3}S$. The $Cd_{1-x}Mn_xS$ (x = 0.1, 0.3, 0.5, 0.7, 0.9) was synthesized through a simple hydrothermal process. Subsequently, Ni was deposited on the surface of $Cd_{0.7}Mn_{0.3}S$ via facile chemical reduction-deposition, in which Lysine and NaBH₄ were used as capping agent and reducing agent, respectively. As shown in Fig. S2, the diffraction peaks of the as-prepared CdS and MnS corresponded to hexagonal CdS (JCPDS no. 80–0006) and α-MnS (JCPDS no. 88–2223), respectively. For $Cd_{1-x}Mn_xS$ solid solutions, the diffraction peak of hexagonal CdS exhibited an obvious shift towards α-MnS with the increase of Mn content [28]. The successive shifted in the X-ray diffraction (XRD) patterns of $Cd_{1-x}Mn_xS$ solid solution indicated that the $Cd_{1-x}Mn_xS$ were not a simple physical combination of CdS and MnS. Moreover, the comparison of (101) characteristic peak showed that the diffraction peak of $Cd_{0.7}Mn_{0.3}S$ shifted toward a higher 2θ angle (0.2°) compared to that of CdS (Fig. S3), implying that the decrease in

lattice parameters (d_{101} value) for $Cd_{0.7}Mn_{0.3}S$ according to Bragg's law. Since the radius of the ion of Mn^{2+} (64 pm) is smaller than that of Cd^{2+} (97 pm), it is considered that the Mn^{2+} is incorporated in the CdS lattice [29–31]. It was noteworthy that with the increase of Ni loading amount, due to the small size of Ni particles, there was no Ni species characteristic peak in the XRD patterns of X% $Ni/Cd_{0.7}Mn_{0.3}S$ and the XRD pattern does not shift compared with the (101) crystal face $Cd_{0.7}Mn_{0.3}S$ in the range of $2\theta= 27–30°$ (Fig. 1a) [32].

X-ray photoelectron spectroscopy (XPS) was conducted to investigate the surface element composition and valence states of the CdS, $Cd_{0.7}Mn_{0.3}S$ and 8% $Ni/Cd_{0.7}Mn_{0.3}S$. According to the full survey spectrum, the main element was Cd, Mn, S and Ni in 8% $Ni/Cd_{0.7}Mn_{0.3}S$ (Fig. S4). As shown in Fig. S5, the Cd 3d and S 2p characteristic peaks of $Cd_{0.7}Mn_{0.3}S$ shift to higher biding energies compared with that of CdS, implying that Mn^{2+} doping decreased electron density of Cd and S atoms [8,12]. As for $Ni/Cd_{0.7}Mn_{0.3}S$, both Cd $3d_{5/2}$ and Cd $3d_{3/2}$ binding energies obviously shift to higher compared with that of $Cd_{0.7}Mn_{0.3}S$ (Fig. 1b), suggesting that the electron may transfer from $Cd_{0.7}Mn_{0.3}S$ to Ni at $Ni/Cd_{0.7}Mn_{0.3}S$ interface [33–36]. Nevertheless, binding energies of Mn $2p_{3/2}$ and Mn $2p_{1/2}$ exhibited obviously change [37], testifying that the strong interaction force formed between Cd and Ni atoms at $Ni/Cd_{0.7}Mn_{0.3}S$ interface (Fig. 1c). Furthermore, the S 2p peaks in the 8% $Ni/Cd_{0.7}Mn_{0.3}S$ shift to higher energy compared with $Cd_{0.7}Mn_{0.3}S$, probably due to the build-in field formed in the energy arrangement of Schottky junction (Fig. 1d) [38,39]. The XRD and XPS results indicated that Ni 2p exhibits lower binding energy in 8% $Ni/Cd_{0.7}Mn_{0.3}S$ than that of metal Ni, indicating that the electrons flowed from to Ni (Fig. S6). As for Ni 2p spectrum of $Ni/Cd_{0.7}Mn_{0.3}S$, the strongest peaks at 853.2 (Ni^0) and 870.7 eV (Ni^0) corresponds to $2p_{3/2}$ and $2p_{1/2}$ binding energies of the metallic Ni (Fig. 1e) [40]. Besides, the peaks at 855.8/860.2 and 873.7/877.0 eV corresponds to Ni^{2+} $2p_{3/2}$ and Ni^{2+} $2p_{1/2}$, respectively (Fig. 1e). Interestingly, a Ni-S peak appeared at the binding energy of 849.9 eV, confirming the formation of Ni-S bond at $Ni/Cd_{0.7}Mn_{0.3}S$ interface [41]. The formation of Ni-S bond at $Ni/Cd_{0.7}Mn_{0.3}S$ interface was further confirmed by Raman spectra (Fig. 1f). The relatively moderate peak corresponding to the $Cd_{0.7}Mn_{0.3}S$ and 8% $Ni/Cd_{0.7}Mn_{0.3}S$ located at 212 cm^{-1} could belonged to multiple phonon scattering. The intense Raman peak at 287 cm^{-1} relatives to the first-order longitudinal (1-LO) optical phonon band of $Cd_{0.7}Mn_{0.3}S$. It is worth mentioning that a new peak located at 550 cm^{-1} appears in 8% $Ni/Cd_{0.7}Mn_{0.3}S$, which can be attributed to the vibrational mode of Ni-S bond [19]. Accordingly, the combination of XPS and Raman results further testified the successfully

construction of chemical-bonded $Ni/Cd_{0.7}Mn_{0.3}S$.

Surface textures and specific surface area (BET) surface area of $Cd_{0.7}Mn_{0.3}S$ and 8% $Ni/Cd_{0.7}Mn_{0.3}S$ were studied using N_2 adsorption/ adsorption isotherm. As shown in Figs. S7a-7b both $Cd_{0.7}Mn_{0.3}S$ and 8% $Ni/Cd_{0.7}Mn_{0.3}S$ exhibited type-IV isotherm with H3 hysteresis loops, indicating their mesoporous and macroporous structure [42]. As shown in Figs. S7c-7d and (Table S1), both $Cd_{0.7}Mn_{0.3}S$ and 8% $Ni/Cd_{0.7}Mn_{0.3}S$ had the similar pore structure while 8% $Ni/Cd_{0.7}Mn_{0.3}S$ possess the higher specific surface area (21.14 $m^2 \cdot g^{-1}$) than that of $Cd_{0.7}Mn_{0.3}S$ (13.86 $m^2 \cdot g^{-1}$), which might attribute to the loading of Ni particles on the surface of $Cd_{0.7}Mn_{0.3}S$ nanorods [43].

As displayed in Fig. 2, scanning electron microscope (SEM) and transmission electron microscope (TEM) were used to further observe the morphological of CdS, $Cd_{0.7}Mn_{0.3}S$ and 8% $Ni/Cd_{0.7}Mn_{0.3}S$. The morphology of all the samples were nanorod-like structures (Fig. 2a-c and Fig. 2d-f). The interplanar spacing of CdS, $Cd_{0.7}Mn_{0.3}S$ and 8% $Ni/Cd_{0.7}Mn_{0.3}S$, corresponding to its (101) crystal plane, as shown in Fig. 2g-i. Obviously, the interplanar crystal spacing of $Cd_{0.7}Mn_{0.3}S$ was reduced comparison to that of CdS, demonstrating that Mn^{2+} is doped into the CdS lattice to form the solid solution. The crystal plane spacing of $Cd_{0.7}Mn_{0.3}S$ did not change after Ni loading because Ni is deposited on the surface of $Cd_{0.7}Mn_{0.3}S$ instead of entering the crystal lattice of $Cd_{0.7}Mn_{0.3}S$ [42]. As seen in Fig. 2i, the distance between two adjacent lattice stripes of the nanoparticle is approximately 0.203 nm, which is compatible with the spacing of (111) plane of metal Ni [44], indicating that Ni particles are successfully loaded on the $Cd_{0.7}Mn_{0.3}S$ surface. The elemental mapping confirmed the co-existence of Cd, Mn, S and Ni elements in 8% $Ni/Cd_{0.7}Mn_{0.3}S$ sample, as well as the uniform dispersion of Ni on the surface of $Cd_{0.7}Mn_{0.3}S$ (Fig. 2j, Fig. S8 and Table S2), which was further testified by ICP (Table S3). Furthermore, the size and morphology of metal Ni on the surface $Cd_{0.7}Mn_{0.3}S$ nano-rod was testified by a 20% $Ni/Cd_{0.7}Mn_{0.3}S$ sample. Obviously, Ni exhibits the cluster loaded on the surface of $Cd_{0.7}Mn_{0.3}S$ nano-rod (Fig. S9).

### 3.2. The photocatalytic properties of 8% $Ni/Cd_{0.7}Mn_{0.3}S$

The HER performance of $Ni/Cd_{0.7}Mn_{0.3}S$ under simulated sunlight irradiation was evaluated using 100 mL Na_2S (0.15 M)/Na_2SO_3 (0.35 M) as sacrifice agent. As shown in Fig. 3a, the HER activities of $Cd_{1-x}Mn_xS$ (x = (0.1, 0.3, 0.5, 0.7, 0.9) solid solution exhibit a volcanic curve along with Mn doping content. As expected, Ni loading further boosted the photocatalytic HER rate of $Cd_{0.7}Mn_{0.3}S$, which follow a
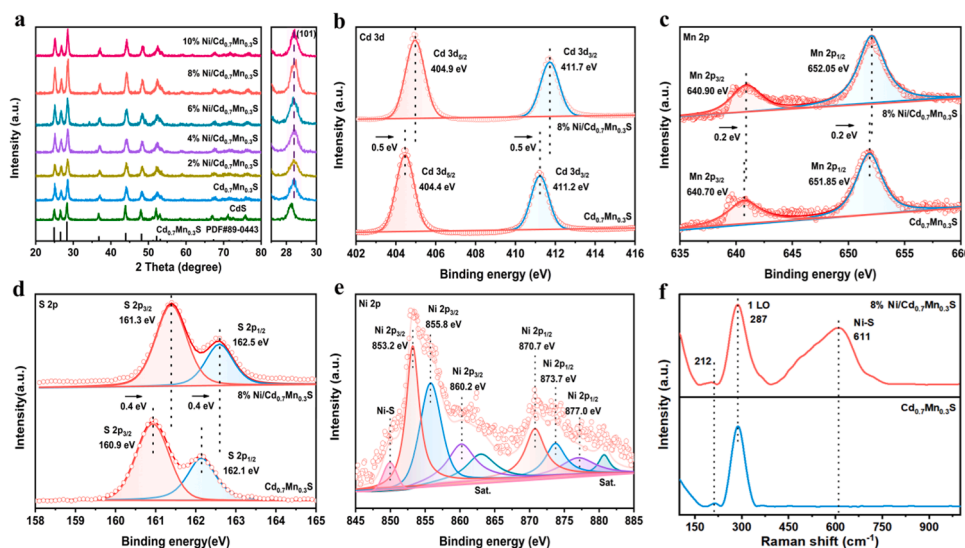
Fig. 1. (a) XRD pattern of x% $Ni/Cd_{0.7}Mn_{0.3}S$ (x = 0, 2, 4, 6, 8, 10) and their partial enlargement over 28°~30° of all samples; XPS spectra of (b) Cd 3d, (c) Mn 2p, (d) S 2p and (e) Ni 2p for $Cd_{0.7}Mn_{0.3}S$ and 8% $Ni/Cd_{0.7}Mn_{0.3}S$; (f) Raman spectra of $Cd_{0.7}Mn_{0.3}S$ and 8% $Ni/Cd_{0.7}Mn_{0.3}S$.
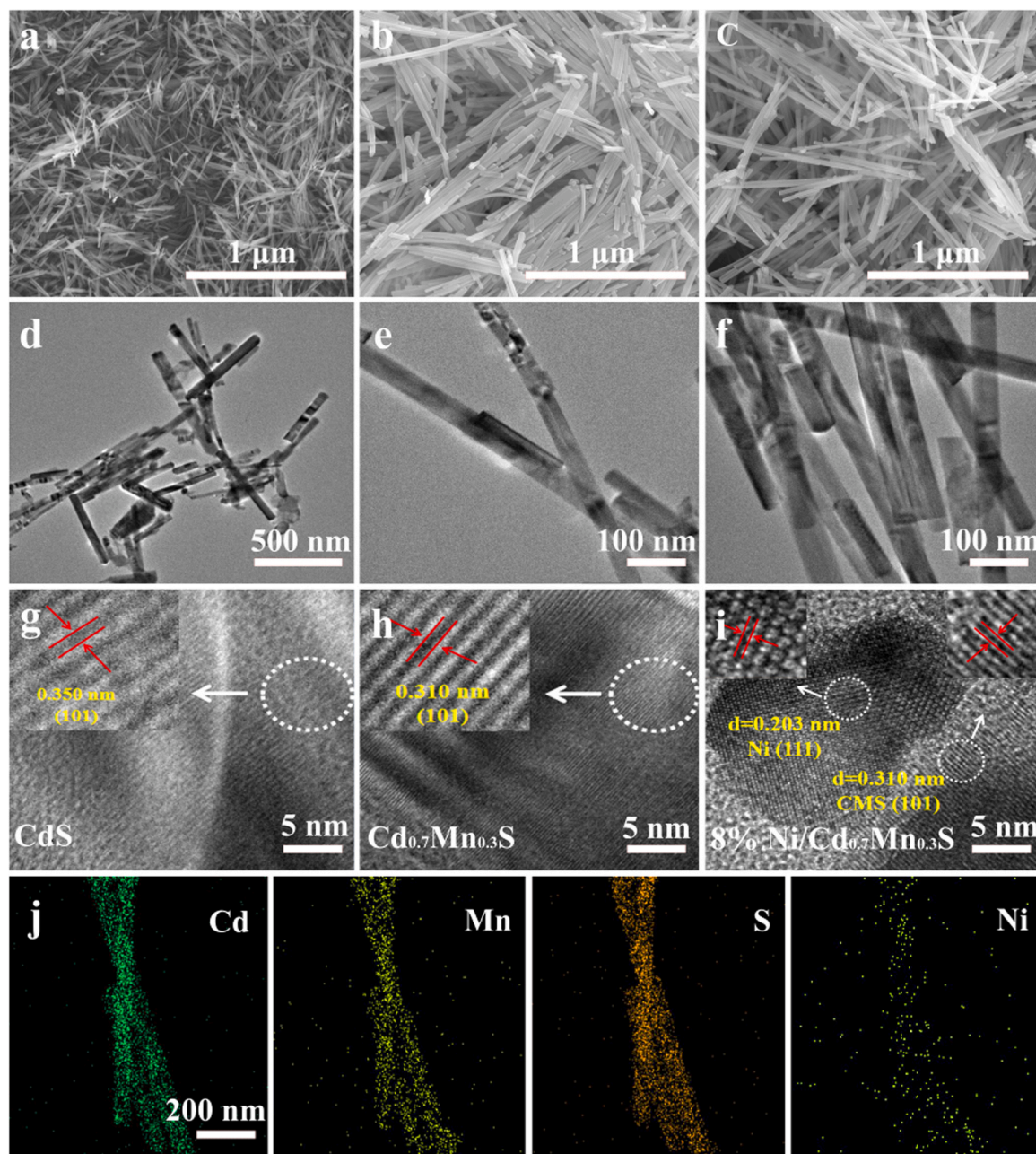
Fig. 2. SEM of (a) CdS, (b) $Cd_{0.7}Mn_{0.3}S$ and (c) 8% $Ni/Cd_{0.7}Mn_{0.3}S$; TEM of (d) CdS; (e) $Cd_{0.7}Mn_{0.3}S$ and (f) 8% $NiCd_{0.7}Mn_{0.3}S$; (g-i) Crystal spacing diagram of CdS, $Cd_{0.7}M_{n0.3}S$ and 8% $Ni/Cd_{0.7}Mn_{0.3}S$; (j) Corresponding energy dispersive X-Ray (EDX) mapping of 8% $Ni/Cd_{0.7}Mn_{0.3}S$.

volcanic curve along with Ni loading. The 8% $Ni/Cd_{0.7}Mn_{0.3}S$ exhibited the optimal HER activity (25 mmol·g^{-1}·h^{-1}) (Fig. 3b and Fig. S10), which was 20 times higher than that of $Cd_{0.7}Mn_{0.3}S$. And when Ni deposition was greater than 8%, the photocatalytic HER of $Ni/Cd_{0.7}Mn_{0.3}S$ decreased. It could also be observed from Fig. 3c that the photocatalytic HER activity of 8% $Ni/Cd_{0.7}Mn_{0.3}S$ was increased linearly along with light irradiation time, implying its excellent stability. In addition, 8% $Ni/Cd_{0.7}Mn_{0.3}S$ exhibited the twice HER activity than that of 8% $NiS/Cd_{0.7}Mn_{0.3}S$ (Fig. S11), further testifying that chemical bond (Ni-S) at $Ni/Cd_{0.7}Mn_{0.3}S$ Schottky junction interface can promote photocatalytic HER performance. The AQY plots of 8% $Ni/Cd_{0.7}Mn_{0.3}S$ was displayed in Fig. 3d. The AQY values of 8% $Ni/Cd_{0.7}Mn_{0.3}S$ at 365, 380, 400, 420, 450 and 500 nm were calculated to be 1.89%, 0.60%, 0.46%, 0.36% and 0.12%, respectively. The AQY@ 420 nm of 8% $Ni/Cd_{0.7}Mn_{0.3}S$ Schottky junction is at the general level compared to previous reported photocatalysts (Table S4). After the photocatalytic HER

for 24 h, the XPS, XRD, TEM and SEM of 8% $Ni/Cd_{0.7}Mn_{0.3}S$ Schottky junction was basically the same as before the reaction, which further confirmed its superior stability (Figs. S12-14).

Selective oxidative dehydrogenation of aromatic alcohol-based platform molecules to aromatic aldehyde/ketone is one of the most important value-added reactions. To further explore the performance of as-constructed chemical-bonded $Ni/Cd_{0.7}Mn_{0.3}S$, the photocatalytic HER was coupled with aromatic alcohol selective oxidation, in which the aromatic alcohol was acted as alternatives to sacrificial agents as well as converting into high-valued products, as shown in Fig. S15 and Fig. 3e. It can be seen from Fig. 3e, that the HER activity and benzaldehyde (BAD) production rate is negligible in benzyl alcohol/H_2O mixture with $Cd_{0.7}Mn_{0.3}S$ as photocatalyst. As for x% $Ni/Cd_{0.7}Mn_{0.3}S$ (x = 0, 2, 4, 6, 8,10), 8% $Ni/Cd_{0.7}Mn_{0.3}S$ exhibit the optimal activity of both HER and BAD production rate, which reach 2.94 mmol·g^{-1}·h^{-1} and 2.88 mmol·g^{-1}·h^{-1}, respectively (Fig. S15 and Fig. 3e). The BA
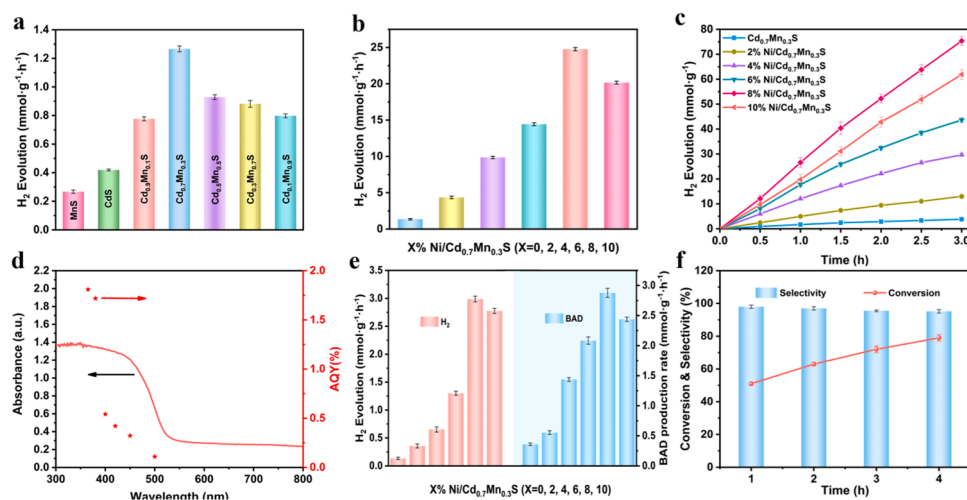
Fig. 3. Photocatalytic hydrogen production activity of (a) MnS, CdS, $Cd_{1-x}Mn_xS$ and (b,c) x% $Ni/Cd_{0.7}Mn_{0.3}S$ (x = 0, 2, 4, 6, 8, 10); (d) UV–vis absorption spectrum of 8% $Ni/Cd_{0.7}Mn_{0.3}S$ (left axis) and AQY under different wavelength of 8% $Ni/Cd_{0.7}Mn_{0.3}S$ (right axis); (e) Photocatalytic H_2 activity and BAD production rate of different catalysts under visible light irradiation; (f) BA conversion rate and BAD selectivity over 8% $Ni/Cd_{0.7}Mn_{0.3}S$.

conversion rate and BAD selectivity are 77% and 98% after four hours of visible light irradiation, respectively (Fig. 3f and Fig. S16). The effect of para-substituents (-CH$_3$, -OCH$_3$, -Br, -NO$_2$) on the selective oxidation performance of BA was also investigated (Fig. S17 and Table 1). As can be seen from Table 1 that both electron-donating groups (-CH$_3$, -OCH$_3$) and withdrawing groups (-Br, -NO$_2$) can seriously affect the selective oxidation of BA on 8% $Ni/Cd_{0.7}Mn_{0.3}S$. The electron-donating groups promote the conversion of BA, while the electron withdrawing groups contrarily suppress BA oxidation. In principle, the electron-donating para-substituents can increase the electron cloud density of aromatic alcohols, which is beneficial to produce and stabilize the radical intermediate ($RC_6H_5\dot{C}HOH$) via cleavage of α_{C-H} bond and further transfer to BAD [45–47]. Furthermore, both ortho- and meta-substituents decrease the conversion and selectivity of photocatalytic BA selcective oxidation coupling HER performance (Fig. S18, Table S5 and Table S6). The present paper mainly focused on construction the efficient chemical-bonded

Ni/$Cd_{0.7}Mn_{0.3}S$ Schottky junction interface, which exhibit the excellent performance in photocatalytic value-added conversion of organic platform molecules with the similar benzyl alcohol structure (such as benzyl alcohol, 5-hydroxymethylfurfural, vanillyl alcohol, *etc*) coupling HER (Fig. 4, Fig. S19 and Fig. S20).

3.3. Study of carrier dynamics

The $Cd_{1-x}Mn_xS$ solid solution is constructed by partly substituting Cd by Mn in CdS. As shown in Fig. S21 and Fig. S22, the energy band-gap structure of $Cd_{1-x}Mn_xS$ solid solution can be accurately regulated by the content of Mn. The optical properties of $Cd_{0.7}Mn_{0.3}S$ and Ni/$Cd_{0.7}Mn_{0.3}S$ were investigated by UV–vis diffuse reflection spectrum displayed (Fig. 5a and Fig. S23). The absorption edge and band gap of $Cd_{0.7}Mn_{0.3}S$ solid solution was approximately 535 nm and 2.43 eV, respectively (Fig. 5a). The formation of chemical-bonded Ni/

Table 1
Selective oxidation of para-substituted benzyl alcohol.

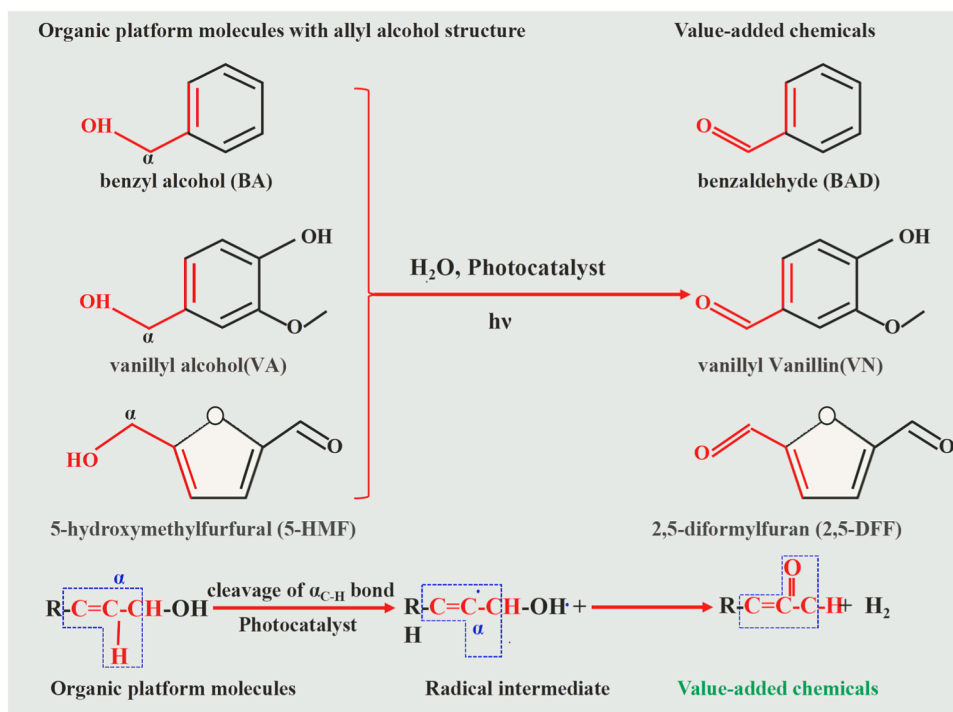| Entry	Substrate	Product	Conv. (%)	Sel. (%)
1	HO—CH$_2$—C$_6$H$_4$—H	O=CH—C$_6$H$_4$—H	77	98
2	HO—CH$_2$—C$_6$H$_4$—CH$_3$	O=CH—C$_6$H$_4$—CH$_3$	82	95
3	HO—CH$_2$—C$_6$H$_4$—OCH$_3$	O=CH—C$_6$H$_4$—OCH$_3$	79	97
4	HO—CH$_2$—C$_6$H$_4$—Br	O=CH—C$_6$H$_4$—Br	59	85
5	HO—CH$_2$—C$_6$H$_4$—NO$_2$	O=CH—C$_6$H$_4$—NO$_2$	30	77

Fig. 4. The typical value-added of organic platform molecules with benzyl alcohol structure.

$Cd_{0.7}Mn_{0.3}S$ Schottky junction leads to the higher valence band maximum (VBM) than that of $Cd_{0.7}Mn_{0.3}S$, resulting in the decrease of gap width, and the red-shift of absorption edge, which was contribute to the increase of the number of photogenerated carriers and the improvement of the photocatalytic HER activity of the catalyst. The band structure of $Cd_{0.7}Mn_{0.3}S$ and 8% $Ni/Cd_{0.7}Mn_{0.3}S$ were elucidated by Mott-Schottky test and valence band XPS spectra anlysis. The Mott-Schottky plots of $Cd_{0.7}Mn_{0.3}S$ (Fig. 5b) presented a positive slope, revealing its n-type semiconductor feature [48]. The flat band potential (V_{fb}) of $Cd_{0.7}Mn_{0.3}S$ is determined to be -1.61 V ($\mathbf{E_{NHE}/V = E^0_{Ag/AgCl}} + \mathbf{0.197}$). For n-type semiconductors, the conduction band minimum (CBM) position is generally negative 0.2–0.3 V over the V_{fb}. Thus, the CBM of $Cd_{0.7}Mn_{0.3}S$ could be also calculated to be -1.41 V based on the empirical formula ($E_{CBM} = E_{VBM} - E_g$) [49]. The corresponding VBM of $Cd_{0.7}Mn_{0.3}S$ were estimated to be 1.02 V from the VB-XPS spectra (inset in Fig. 5b). The carrier density is calculated by Mott-Schottky, as shown in Fig. 5b and Fig. S24. Because of the higher donor density and faster charge transfer, the slope of 8% $Ni/Cd_{0.7}Mn_{0.3}S$ is smaller than that of $Cd_{0.7}Mn_{0.3}S$. The slopes of Mott-Schottky diagram can be used to compute the carrier densities (N_d) of the samples by using the following equation [50], $N_d = \frac{2}{e_0\varepsilon\varepsilon_0}[\frac{d(\frac{1}{C^2})}{dV}]^{-1}$, where e_0 is the electron charge (1.6×10^{-19} C), ε is the rutile $Cd_{0.7}Mn_{0.3}S$ and 8% $Ni/Cd_{0.7}Mn_{0.3}S$ dielectric constant, ε_0 is the vacumm dielectric constant (8.86×10^{-12} F·m^{-1}) and V is the electrode bias. The N_d is calculated to be 2.41×10^{21} cm^{-3} and 2.96×10^{21} cm^{-3} of $Cd_{0.7}Mn_{0.3}S$ and 8% $Ni/Cd_{0.7}Mn_{0.3}S$, respectively.

The carrier separation/transfer dynamics of photocatalyst was investigated by the transient photocurrent, electrochemical impedance spectroscopy (EIS), steady-state photoluminescence spectra (PL) and time-resolved photoluminescence decay spectra (TR-PL). In the Fig. 5c, the photocurrent density of 8% $Ni/Cd_{0.7}Mn_{0.3}S$ (0.48 μA/cm^2) is six-fold that of $Cd_{0.7}Mn_{0.3}S$ (0.08 μA/cm^2). The EIS result indicated that $Cd_{0.7}Mn_{0.3}$ and 8% $Ni/Cd_{0.7}Mn_{0.3}S$ electrodes performed the similar ohmic resistance (R_S), whereas the 8% $Ni/Cd_{0.7}Mn_{0.3}S$ exhibited lower charge transfer resistance (R_P) than that of $Cd_{0.7}Mn_{0.3}S$ (Fig. 5d). The lower R_P of 8% $Ni/Cd_{0.7}Mn_{0.3}S$ attributed to the formed Ni-S bond at Ni/$Cd_{0.7}Mn_{0.3}S$ interface, which can boost the spatial separation of

photogenerated electron/holes for reduction/oxidation-half reactions [51]. The photoluminescence (PL) properties shown that 8% $Ni/Cd_{0.7}Mn_{0.3}S$ exhibited much weaker intensity than that of $Cd_{0.7}Mn_{0.3}S$ (Fig. 5e), indicating that the photogenerated carriers recombination was prominently hindered by Ni loading. As shown in Fig. 5 f and Table S7, the TR-PL spectra further revealed that carrier photogenerated carriers life-time of 8% $Ni/Cd_{0.7}Mn_{0.3}S$ (0.911 ns) was higher than that of $Cd_{0.7}Mn_{0.3}S$ (0.680 ns) due to the formation of chemical-bonded $Ni/Cd_{0.7}Mn_{0.3}S$ Schottky junction [52]. As depicted in Fig. 4 g, the band bending at the semiconductor/electrolyte interface pushed electrons away from the interface while attracting holes (inset in Fig. 5 g), which shows how the V_{fb} of $Cd_{0.7}Mn_{0.3}S$ becomes slightly negative under light irradiation compared with the dark. Due to the large recombination of electron/hole pairs at the $Cd_{0.7}Mn_{0.3}S$ surface, the shift of V_{fb} is small. After the introduction of Ni (Fig. 5 h), the V_{fb} (−1.58 V vs NHE) of $Cd_{0.7}Mn_{0.3}S$ shows negative shift than that of 8% $Ni/Cd_{0.7}Mn_{0.3}S$ (−1.65 V vs NHE), which is ascribed to the formation of Schottky heterojunction. Furthermore, the photogenerated electrons could transfer to Ni, which is advantageous for lowering the charge recombination, resulted in a larger negative shift of the V_{fb} when 8% $Ni/Cd_{0.7}Mn_{0.3}S$ was irradiated (inset in Fig. 5 h) [53]. In conclusion, the construction of 8% $Ni/Cd_{0.7}Mn_{0.3}S$ significantly reduces the electron transfer hindrance at the compact interface, which accelerates the transfer and migration of photogenerated electrons to Ni, thus significantly promoting the efficient separation of photogenerated electrons. The surface photovoltage spectra (SPV) was applied to further prove that the Schottky junction effectively increases the separation efficiency of electron / hole pairs. As shown in Fig. 5i, the SPV response of all samples is positive in the wavelength range from 200 to 800 nm, indicating the characteristics of n-type semiconductors, while the photogenerated electrons transfer to the bulk and the photogenerated holes transfer to the semiconductor surface. The positive photovoltage signal can be observed in the surface photovoltage (SPV) spectra of $Cd_{0.7}Mn_{0.3}S$ and 8% $Ni/Cd_{0.7}Mn_{0.3}S$, but the SPV signal of 8% $Ni/Cd_{0.7}Mn_{0.3}S$ is lower than that of $Cd_{0.7}Mn_{0.3}S$ due to the loaded Ni accelerating the photogenerated carrier migration. That is to say, the loaded Ni receive the photogenerated electrons from $Cd_{0.7}Mn_{0.3}S$ and reduce the
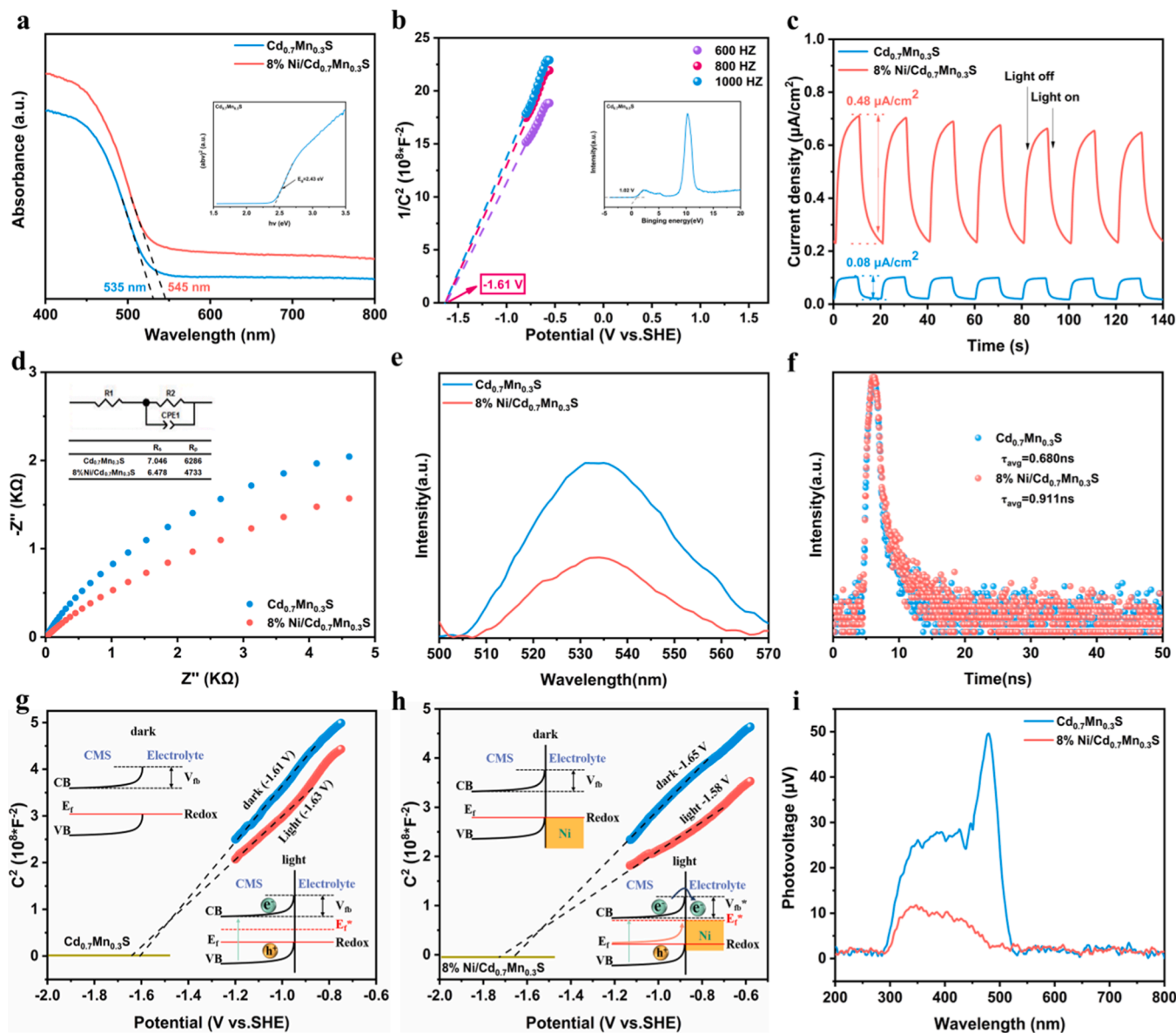
Fig. 5. (a) UV-Vis spectra of $Cd_{0.7}Mn_{0.3}S$ and 8% $Ni/Cd_{0.7}Mn_{0.3}S$ (embed map is bandgap of $Cd_{0.7}Mn_{0.3}S$); (b) Mott-Schottky plots of $Cd_{0.7}Mn_{0.3}S$ (embed map is VB-XPS spectra of $Cd_{0.7}Mn_{0.3}S$); (c) Transient photocurrent response curves; (d) Nyquist plots of electrochemical impedance spectroscopy; (e) Steady-state photoluminescence spectra of all samples; (f) Time-resolved photoluminescence decay spectra of the as-prepared samples; Mott-Schottky plots of (g) $Cd_{0.7}Mn_{0.3}S$ and (h) 8% $Ni/Cd_{0.7}Mn_{0.3}S$ under dark and light conditions; (i) Surface of photovoltage (SPV) measurement of $Cd_{0.7}Mn_{0.3}S$ and 8% $Ni/Cd_{0.7}Mn_{0.3}S$.

photogenerated carrier recombination under the interface electric field induced by Schottky junction [54].

3.4. Identification of active species in photocatalytic reactions

In order to investigate the active species in the photocatalytic selective oxidation BA coupling HER over 8% $Ni/Cd_{0.7}Mn_{0.3}S$, IPA, BQ, 2Na-EDTA and $AgNO_3$ were employed as scavengers to capture hydroxyl radicals (·OH), superoxide radical (·O_2^-), photogenerated hole (h^+) and electron (e^-), respectively. As shown in Fig. 6a, the photocatalytic selective oxidation BA and HER activity remained unchanged in the presence of IPA and 2Na-EDTA, while BQ and $AgNO_3$ suppressed the HER and BA selective oxidation activity significantly, indicated that·O_2^- and e^- play the main role in the photocatalytic reaction. The above experiments were also carried out in the system of photocatalytic HER in the presence of Na_2S/Na_2SO_3, suggesting that·O_2^- and e^- were the main active species (Fig. S25). According to Fig. 6b-f, none of the samples exhibits an in-situ electron spin resonance (ESR) signal under dark

conditions, proving that the reaction is photo-driven process. The presence of the ESR signal for·O_2^-,·OH and·C under light, and their intensity gradually increased with the irradiation time. It is proved that the active substances (·O_2^-,·OH and·C) are produced in the photocatalytic redox coupling. Fig. 6b-e show that the in-situ ESR signals of DMPO-·O_2^- and DMPO-·OH for 8% $Ni/Cd_{0.7}Mn_{0.3}S$ are stronger than those of $Cd_{0.7}Mn_{0.3}S$, showing that Ni decoration enhanced the production of active species, which is consistent with the high conversion of BA and yield of H_2. Now that the CBM of $Cd_{0.7}Mn_{0.3}S$ (−1.58 V) is higher than the redox potential of E (O_2/·O_2^-) = −0.33 V, the electrons on the CBM of $Cd_{0.7}Mn_{0.3}S$ have sufficient ability to reduce O_2 to·O_2^-. Simultaneously, the VBM of $Cd_{0.7}Mn_{0.3}S$ is 0.88 V, as well as the redox potentials of H_2O /·OH and OH^- /·OH are 2.37 V and 1.99 V, respectively [55]. Thermodynamically, both H_2O and OH^- can not be directly oxidized to·OH. Accordingly, the produced·OH may be attributed to the transformation from·O_2^- [6]. As so as to research the mechanism of BA photocatalytic dehydrogenation oxidation, the active species were monitored by in-situ
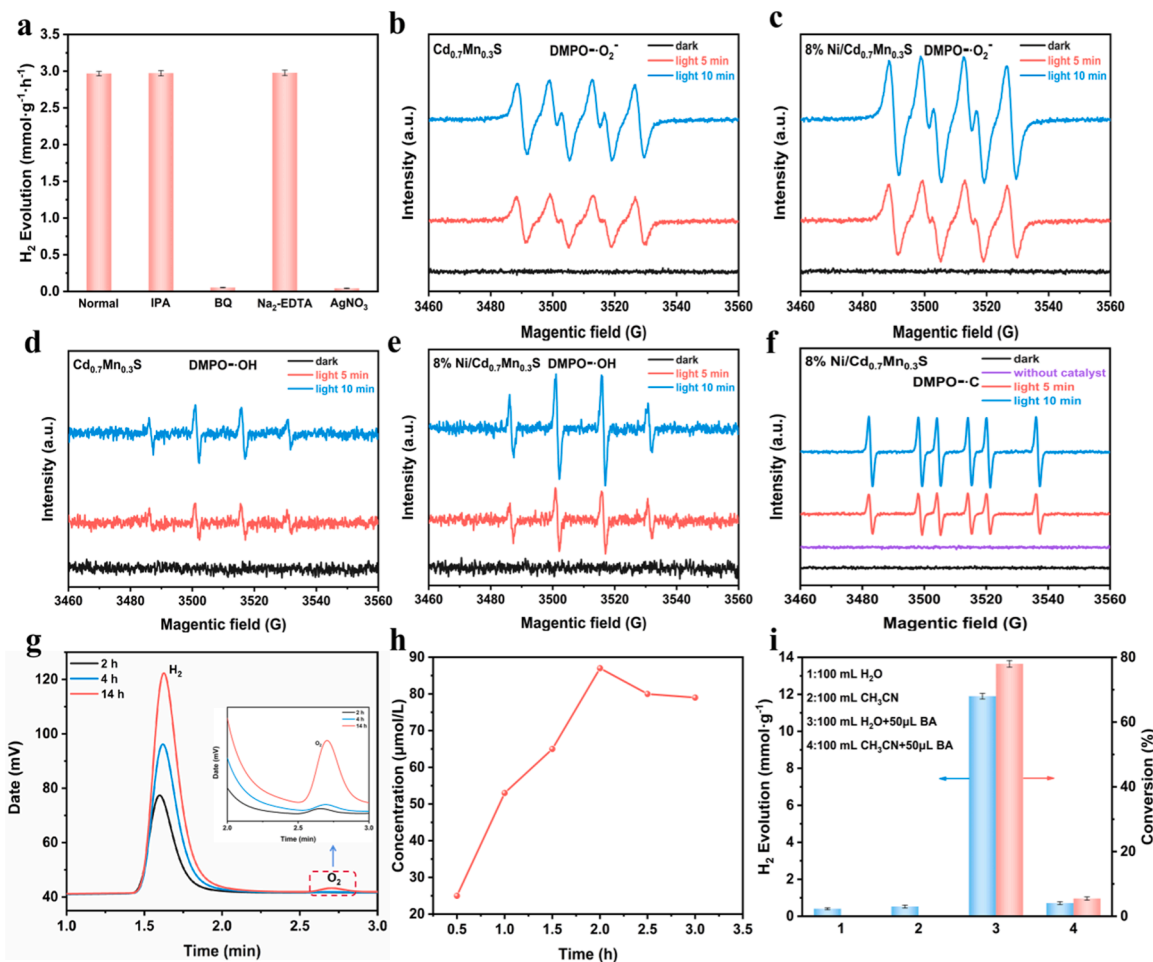
Fig. 6. Validation of active species. (a) The main active species captured experiment of 8% Ni/Cd$_{0.7}$Mn$_{0.3}$S in benzyl alcohol solution; ESR spectra of (b) DMPO-·O$_2^-$ and (b) DMPO-·OH for Cd$_{0.7}$Mn$_{0.3}$S; (c) DMPO-·O$_2^-$, (e) DMPO-·OH and (f) DMPO-·C for 8% Ni/Cd$_{0.7}$Mn$_{0.3}$S in benzyl alcohol aqueous solution; (g) Chromatogram of hydrogen and oxygen production using 8% Ni/Cd$_{0.7}$Mn$_{0.3}$S; (h) H$_2$O$_2$ production over time (8% Ni/Cd$_{0.7}$Mn$_{0.3}$S, 200 mg); (i) Conversion of benzyl alcohol and H$_2$ evolution using 8% Ni/Cd$_{0.7}$Mn$_{0.3}$S photocatalyst under different conditions.

ESR. As shown in Fig. 6f, carbon-anion radicals ($RC_6H_5\overset{\bullet}{C}HOH$) was light-dependent, which are the main intermediates in selective dehydrogenation of benzyl alcohol by the cleavage of α$_{C-H}$ bond [47].

The above-mentioned results revealed that·O$_2^-$ and e⁻ played a decisive role in the photocatalytic BA oxidation coupling HER. The generated O$_2$ was verified by gas chromatography, which is far less than half of H$_2$ as exhibited in Fig. 6g. The yield of O$_2$ was essentially unaltered while the amount of H$_2$ was steadily increased under light irradiation (insert picture in Fig. 6g). Further extending the reaction time, a stronger O$_2$ peak appear, which was attributed to that the generated O$_2$ was no longer consumed by BA. So as to verify the generation of O$_2$ in the photocatalysis reaction, the concentration of hydrogen peroxide (H$_2$O$_2$) in the conversion of BA was further analyzed. It revealed that with the increase of irradiation, the concentration of H$_2$O$_2$ gradually increasing and then reached equilibrium, which indirectly proved that O$_2$ was indeed produced in the photocatalytic reaction other than dissolved oxygen (Fig. 6h and Fig. S26). Besides, it can be inferred that the·OH is formed via an indirectly process (O$_2$ + e⁻→·O$_2^-$,·O$_2^-$ + 2 H⁺ + e⁻→H$_2$O$_2$, H$_2$O$_2$ + e⁻→·OH + OH⁻) [55]. Furthermore, photocatalytic selective oxidation of BA coupling HER was conducted by employing acetonitrile as solvent, as shown in Fig. 6i. Without H$_2$O, both the HER rate and conversion of BA of Ni/Cd$_{0.7}$Mn$_{0.3}$S are negligible, confirming that water played a decisive role in promoting the photocatalytic BA oxidation/HER coupling reaction. The presence of BA may change the ionization balance of water, thus promote HER half-reaction. This

further confirm that oxygen (O$_2$) was produced by OER. The as-produced O$_2$ absorbed on the surface of photocatalyst can capture conduction-band electron to form superoxide radical (·O$_2^-$), which further oxidize BA to form BAD. The reduction of water produces a large amount of hydrogen, while the α$_{C-H}$ bond dehydrogenation of BA only forms a small amount of hydrogen.

3.5. Mechanism of photocatalytic selective oxidation of aromatic alcohol coupling HER

The charge transfer at the Ni/Cd$_{0.7}$Mn$_{0.3}$S Schottky junction is studied by calculating the work function (φ). Now that the φ of Cd$_{0.7}$Mn$_{0.3}$S (φ$_s$, 4.89 eV) is less than Ni (φ$_m$, 5.14 eV). The Schottky junction can be formed when Ni is in contact with Cd$_{0.7}$Mn$_{0.3}$S, and the electrons on the interface are transformed from Cd$_{0.7}$Mn$_{0.3}$S to Ni and the process is irreversible (Fig. 7a and Fig. 7b). The charge density difference of Ni/Cd$_{0.7}$Mn$_{0.3}$S Schottky junction at the interface is simulated in Fig. 7c and Fig. S27, where yellow and blue indicate areas of charge accumulation and depletion, respectively. The results show that the electrons transferring from Cd$_{0.7}$Mn$_{0.3}$S to Ni along the as-formed Ni-S bond induces a region of space charge between Schottky junctions, which was consistent with XPS result (Fig. 1b~1e). In addition, according to the calculation of interface electrostatic potential, the direction of the interface electric field (IEF) is directed from CMS to Ni, with a Ni-CMS interface energy barrier of 4.51 eV (Fig. S28) [56–58].

Accordingly, the formation of chemical-bonded Ni/Cd$_{0.7}$Mn$_{0.3}$S
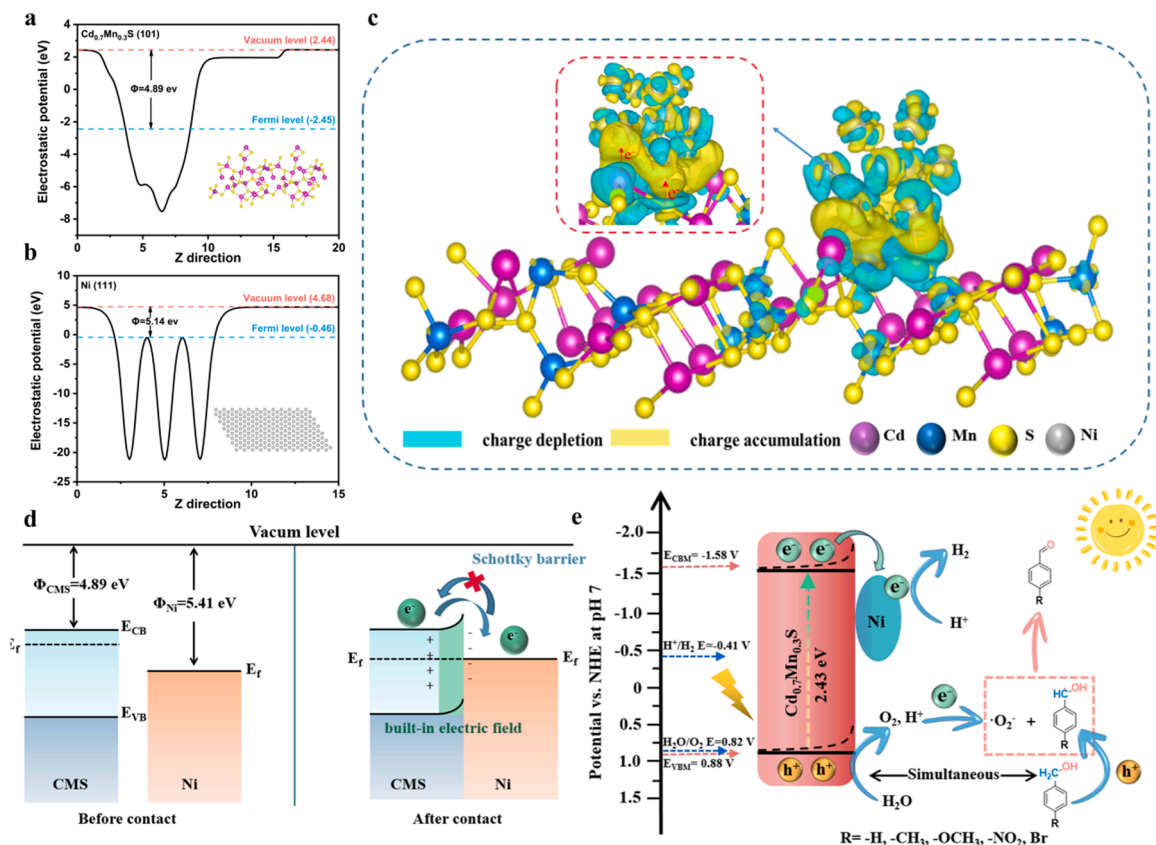
Fig. 7. The electrostatic potentials of (a) $Cd_{0.7}Mn_{0.3}S$ (101) facet and (b) Ni (111) facet; (c) The charge density difference of $Ni/Cd_{0.7}Mn_{0.3}S$; (d) The formation mechanism of chemical-bonded $Ni/Cd_{0.7}Mn_{0.3}S$ Schottky junction; (e) Schematic diagram of 8% $Ni/Cd_{0.7}Mn_{0.3}S$ Schottky junction photocatalytic selective dehydrogenation oxidation of BA coupled with H_2 production.

Schottky junction and the feasible mechanism of photocatalytic HER coupling $RC_6H_5CH_2OH$ (BA, R= -CH₃, -OCH₃, -NO₂, Br, *etc*.) selective oxidation to BAD was also proposed. As shown in Fig. S29 and Fig. 7d, the work function of the metal Ni (ϕ_m=5.14 eV) is larger than $Cd_{0.7}Mn_{0.3}S$ (ϕ_s =4.89 eV), the electrons tend to transfer from $Cd_{0.7}Mn_{0.3}S$ to the Ni until the Fermi level is aligned [59]. At the $Ni/Cd_{0.7}Mn_{0.3}S$ interface, where the Ni carries negative charged and the $Cd_{0.7}Mn_{0.3}S$ is positively charged at its surface due to electrostatic induction, a Helmholtz double layer will form under equilibrium. It is can not be effectively to shield the electric field between Ni and $Cd_{0.7}Mn_{0.3}S$ interfaces owing to the low concentration of free carriers in the $Cd_{0.7}Mn_{0.3}S$. This results the free charge carrier concentration near the $Cd_{0.7}Mn_{0.3}S$ surface to be depleted compared with the bulk. Since ϕ_m (5.14 eV) > ϕ_s (4.89 eV), the negatively charged Helmholtz layer located in the Ni exhibits repulsive force on the electron in $Cd_{0.7}Mn_{0.3}S$, its potential energy rises and the bands bend upward toward the interface and form a Schottky barrier at the $Ni/Cd_{0.7}Mn_{0.3}S$ interface, in which metallic nickel chemical bonded on $Cd_{0.7}Mn_{0.3}S$ nanorods via the formation Cd-S-Ni bond act as admirable electron acceptors as well as provide a wide range of active sites for proton (H^+) reduction.
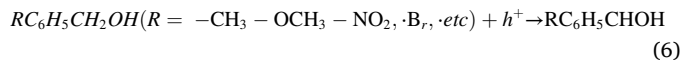
Fig. 7e displays the reaction mechanism of photocatalytic selective oxidation of BA coupled with HER on chemical-bonded $Ni/Cd_{0.7}Mn_{0.3}S$ Schottky junction, which primarily includes the following steps: i) Under the irradiation of visible light, the $Cd_{0.7}Mn_{0.3}S$ is excited to produce holes/electron pairs. The transfer of electrons from the CBM of the $Cd_{0.7}Mn_{0.3}S$ to Ni is accelerated due to the formation of Ni-S bond between the metallic nickel and $Cd_{0.7}Mn_{0.3}S$. Meanwhile, the h^+ is accumulated in VBM of $Cd_{0.7}Mn_{0.3}S$ (Eq. 3). ii) The photogenerated h^+ on the VBM of $Cd_{0.7}Mn_{0.3}S$ oxidizes H_2O to O_2 and H^+ (Eq. 4). Simultaneously, α_{C-H} bond of BA will be activated by the h^+ in the VBM of $Cd_{0.7}Mn_{0.3}S$ to

form $RC_6H_5\overset{\bullet}{C}HOH$ radicals and release H^+ by the cleavage of α_{C-H} bond of BA (Eq. 5). The produced O_2 captures electrons from Ni to create $\cdot O_2^-$ (Eq. 6). iii) The $RC_6H_5\overset{\bullet}{C}HOH$ active radicals are oxidized by $\cdot O_2^-$ to form BAD (Eq. 7). iv) The H^+ liberated from BA and H_2O oxidation process are reduced to produce H_2 by photogenerated electrons on Ni (Eq. 8).

Step 1: Carrier generation/spatial separation of chemical-bonded $Ni/Cd_{0.7}Mn_{0.3}S$ Schottky junction

$$Ni/Cd_{0.7}Mn_{0.3}S \rightarrow Ni/Cd_{0.7}Mn_{0.3}S \ (e^- / h^+) \rightarrow Ni \ (e^-)/Cd_{0.7}Mn_{0.3}S \ (h^+) \quad (3)$$
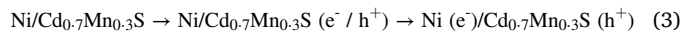
Step 2: H_2O oxidation, BA and O_2 molecule activation reaction

$$H_2O + h^+ \rightarrow H^+ + O_2 + e^- \quad (4)$$

$$O_2 + e^- \rightarrow \cdot O_2^- \quad (5)$$

$$RC_6H_5CH_2OH(R = \ -CH_3 - OCH_3 - NO_2, \cdot B_r, \cdot etc) + h^+ \rightarrow RC_6H_5CHOH \quad (6)$$

Step 3: Photocatalytic selective oxidation of BA to BAD

$$RC_6H_5\overset{\cdot}{C}HOH\cdot + \cdot O_2^- \rightarrow RC_6H_5CHO \quad (7)$$

Step 4: Photocatalytic hydrogen production

$$2\,H^+ + 2e^- \rightarrow H_2 \quad (8)$$

4. Conclusion

In summary, chemical-bonded $Cd_{0.7}Mn_{0.3}S$ and x% $Ni/Cd_{0.7}Mn_{0.3}S$ Schottky junction (x = 0, 2, 4, 6, 8, 10) were designed and constructed by hydrothermal and chemical reduction method for selectively photo-

catalyzed oxidation of BA to BAD combined with H_2 generation. The 8% $Ni/Cd_{0.7}Mn_{0.3}S$ showed admirable photocatalytic performance and chemical steadily, acquiring efficient HER rate (2.94 mmol·g^{-1}·h^{-1}), BAD yields reach 2.88 mmol·g^{-1}·h^{-1} and showed high conversion of BA (77%), while BAD selectivity (99%). The primary element that contributes to improving the photocatalytic performance is the schottky junction formed between Ni and $Cd_{0.7}Mn_{0.3}S$: (i) Ni work as co-catalyst is conducive to enhance the transfer, separation and availability of photo-induced carriers. (ii) Metallic nickel chemical bonded on $Cd_{0.7}Mn_{0.3}S$ nanorods via the formation Ni-S bond act as admirable electron acceptors and a wide range of active sites for H^+ reduction. During the reaction, the water is oxidized to O_2 and H^+, and O_2 act as the electron acceptor to accept electrons from the metal Ni to form·O_2^-. Meanwhile, BA was activated by photogenerated h^+ to produce $RC_6H_5\overset{\bullet}{C}HOH$ active radicals through the cleavage of α_{C-H} bond and produce H^+. The produced $RC_6H_5\overset{\bullet}{C}HOH$ active radicals further reacted with·O_2^- to form BAD. At the Ni active site, the H^+ produced by BA and H_2O oxidation is eventually reduced to produce H_2. When the substituent of benzyl alcohol is the electron donor group, the conversion of benzyl alcohol can be promoted. In this work, non-precious metals and transition metal sulfides were used to construct chemical-bonded Schottky junctions, which achieved high efficiency photocatalytic hydrogen production and high-quality conversion of organic platform molecules. The influence of different substituents on benzyl alcohol conversion was further explored, and a new idea was provided for subsequent biomass conversion.

CRediT authorship contribution statement

Hua Wen: Methodology, Data curation, Writing - Original draft. **Wen Duan**: Investigation, Data curation. **Li Guo**: Resources, Validation. **Qi Wang**: Validation. **Xin Fu**: Validation. **YuHui Wang**: Investigation, Validation. **Ruqi Li**: Data curation, Validation. **Binbin Jin**: Methodology, Formal analysis. **Rui Du**: Visualization, Validation. **Chunming Yang**: Resources, Writing – review & editing. **Danjun Wang**: Conceptualization, Resources, Funding acquisition, Writing – Review & Editing.

Declaration of Competing Interest

The authors declare that they have no known competing financial interests or personal relationships that could have appeared to influence the work reported in this paper (The authors declare no conflict of interest in this manuscript.).

Data availability

Data will be made available on request.

Acknowledgments

Appendix A. Supporting information

Supplementary data associated with this article can be found in the online version at doi:10.1016/j.apcatb.2023.123641.

References

[1] R.Q. Gao, H. He, J.X. Bai, L. Hao, R.C. Shen, P. Zhang, Y.J. Li, X. Li, Pyrene-benzothiadiazole-based polymer/CdS 2D/2D organic/inorganic hybrid s-scheme heterojunction for efficient photocatalytic H_2 evolution, Chinese, J. Struct. Chem. 41 (2022) 2206031–2206038.

[2] C.L. Jiang, H. Wang, Y.Q. Wang, H.B. Ji, All solid-state Z-scheme $CeO_2/ZnIn_2S_4$ hybrid for the photocatalytic selective oxidation of aromatic alcohols coupled with hydrogen evolution, Appl. Catal. B: Environ. 277 (2020) 119235.

[3] L. Xue, Y. Shi, C.P. Huang, Q. Wu, B.B. Chen, W.F. Yao, Zn and Ni dual hydrogen evolution sites integrated onto CdS for effective photocatalytic hydrogen production, J. Colloid Interf. Sci. 635 (2023) 72–82.

[4] J.Q. Huang, S. Yang, S.J. Jiang, C.Z. Sun, S.Q. Song, Entropy-increasing single-atom photocatalysts strengthening the polarization field for boosting H_2O overall splitting into H_2, ACS Catal. 12 (2022) 14708–14716.

[5] H.W. Huang, J.W. Zhao, Y.J. Du, C. Zhou, M.L. Zhang, Z. Wang, Y.X. Weng, J. L. Long, J. Hofkens, J.A. Steele, M.B.J. Roeffaers, Direct z-scheme heterojunction of semicoherent $FAPbBr_3/Bi_2WO_6$ interface for photoredox reaction with large driving force, ACS Nano 14 (2020) 16689–16697.

[6] L.P. Yang, G.H. Dong, D.L. Jacobs, Y.H. Wang, L. Zang, C.Y. Wang, Two-channel photocatalytic production of H_2O_2 over g-C_3N_4 nanosheets modified with perylene imides, J. Catal. 352 (2017) 274–281.

[7] P.F. Li, G. Xiao, Y.L. Zhao, H.J. Su, Tuning the product selectivity of the α-alkylation of ketones with primary alcohols using oxidized titanium nitride photocatalysts and visible light, ACS Catal. 10 (2020) 3640–3649.

[8] Y.G. Lei, K.H. Ng, Y.C. Zhu, Y.Z. Zhang, Z.X. Li, S. Xu, J.Y. Huang, J. Hu, Z. Chen, W.L. Cai, Y.K. Lai, Mo-activated VC as effective cocatalyst for an enhanced photocatalytic hydrogen evolution activity of CdS, Chem. Eng. J. 452 (2023) 139325.

[9] Y.X. Li, W.Z. Zhang, H. Li, T.Y. Yang, S.Q. Peng, C. Kao, W.Y. Zhang, Ni-B coupled with borate-intercalated $Ni(OH)_2$ for efficient and stable electrocatalytic and photocatalytic hydrogen evolution under low alkalinity, Chem. Eng. J. 394 (2020) 124928.

[10] H. Yi, D.L. Huang, L. Qin, G.G. Zeng, G. Lai, M. Cheng, S.J. Ye, B. Song, X.Y. Ren, X. Y. Guo, Selective prepared carbon nanomaterials for advanced photocatalytic application in environmental pollutant treatment and hydrogen production, Appl. Catal. B: Environ. 239 (2018) 408–424.

[11] K. Wang, Y. Li, J. Li, G.K. Zhang, Boosting interfacial charge separation of $Ba_5Nb_4O_{15}$/g-C_3N_4 photocatalysts by 2D/2D nanojunction towards efficient visible-light driven H_2 generation, Appl. Catal. B: Environ. 263 (2020) 117730.

[12] W. Li, F. Wang, X.Y. Liu, Y.Y. Dang, J.Y. Li, T.H. Ma, C.Y. Wang, Promoting body carriers migration of CdS nanocatalyst by N-doping for improved hydrogen production under simulated sunlight irradiation, Appl. Catal. B: Environ. 313 (2022) 121470.

[13] X.L. Hao, X.S. Chu, X.Y. Liu, W. Li, Synergetic metal-semiconductor interaction: single-atomic Pt decorated CdS nano-photocatalyst for highly water-to-hydrogen conversion, J. Colloid Interf. Sci. 621 (2022) 160–168, 621.

[14] Y. Yang, J.S. Wu, B. Cheng, L.Y. Zhang, A.A. Al-Ghamdi, S. Wageh, Y.J. Li, Enhanced photocatalytic H_2-production activity of CdS nanoflower using single atom Pt and graphene quantum dot as dual cocatalysts, Chinese, J. Struct. Chem. 41 (2022) 2206006–2206014.

[15] G.Q. Han, Y.H. Jin, R.A. Burgess, R.N.E Dickenson, X.M. Cao, Y.J. Sun, Visible-light-driven valorization of biomass intermediates integrated with H2 production catalyzed by ultrathin Ni/CdS Nanosheets, J. Am. Chem. Soc. 139 (2017) 15584–15587.

[16] H. Li, Z.Q. Wang, Y.H. He, S.G. Meng, Y. Xu, S.F. Chen, X.L. Fu, Rational synthesis of $Mn_xCd_{1-x}S$ for enhanced photocatalytic H_2 evolution: effects of S precursors and the feed ratio of Mn/Cd on its structure and performance, J. Colloid Interf. Sci. 535 (2019) 469–480.

[17] X.M. Liu, B.Q. Wu, X.Y. Chen, L.S. Yan, H.Q. Guo, K.X. Li, L.P. Xu, J. Lin, A novel hierarchical $Bi_2MoO_6/Mn_{0.2}Cd_{0.8}S$ heterostructured nanocomposite for efficient visible-light hydrogen production, Int. J. Hydrog. Energy 45 (2020) 2884–2895.

[18] X.L. Yin, G.Y. He, B. Sun, W.J. Jiang, D.J. Xue, A.D. Xia, L.J. Wan, J.S. Hu, Rational design and electron transfer kinetics of MoS_2/CdS nanodots-on-nanorods for efficient visible-light-driven hydrogen generation, Nano Energy 28 (2016) 319–329.

[19] J. Wang, Y.A. Zhang, X.X. Wang, W.Y. Su, Simultaneous enhancements in photoactivity and anti-photocorrosion of Z-scheme $Mn_{0.25}Cd_{0.75}S/WO_3$ for solar water splitting, Appl. Catal. B: Environ. 268 (2020) 118444.

[20] M. Yuan, W.H. Zhou, D.X. Kou, Z.J. Zhou, Y.N. Meng, S.X. Wu, Cu_2ZnSnS_4 decorated CdS nanorods for enhanced visible-light-driven photocatalytic hydrogen production, Int. J. Hydrog. Energy 43 (2018) 20408–20416.

[21] H.Z. Zhang, Y.M. Dong, S. Zhao, G.L. Wang, P.P. Jiang, J. Zhong, Y.F. Zhu, Photochemical preparation of atomically dispersed nickel on cadmium sulfide for superior photocatalytic hydrogen evolution, Appl. Catal. B Environ. 261 (2020) 118233.

[22] N. Xiao, S.S. Li, X.L. Li, L. Ge, Y.Q. Gao, N. Li, The roles and mechanism of cocatalysts in photocatalytic water splitting to produce hydrogen, Chin. J. Catal. 41 (2020) 642–671.

[23] Y.D. Sun, C.Y. Xu, H.Y. Ma, G.J. Li, L.L. Chen, Y.F. Sun, Z.Q. Chen, P.F. Fang, Q. Fu, C.X. Pan, Synthesis of flower-liked twin crystal ternary $Ni/NiS/Zn_{0.2}Cd_{0.8}S$ catalyst for highly efficient hydrogen production, Chem. Eng. J. 406 (2021) 126878.

[24] L. Cheng, Q.J. Xiang, Y.L. Liao, H.W. Zhang, CdS-based photocatalysts, Energy Environ. Sci. 11 (2018) 1362–1391.

[25] Y. Zhang, Z.R. Liu, C.Y. Guo, T.X. Chen, C. Guo, Y. Lu, J.D. Wang, CdS(ZB)/CdS (WZ)/Ni-BTC photocatalytic selective oxidation of benzyl alcohol to benzaldehyde coupled with hydrogen evolution, Appl. Surf. Sci. 571 (2022) 151284.

[26] V. Kumar, N. Singh, S. Jana, S.K. Rout, R.K. Dey, G.P. Singh, Surface polar charge induced Ni loaded CdS heterostructure nanorod for efficient photo-catalytic hydrogen evolution, Int. J. Hydrog. Energy 46 (2021) 16373–16386.

[27] C.H. Deng, F. Ye, T. Wang, X.H. Ling, L.L. Peng, H. Yu, K.Z. Ding, H.M. Hu, Q. Dong, H.R. Le, Y.S. Han, Developing hierarchical CdS/NiO hollow heterogeneous architectures for boosting photocatalytic hydrogen generation, Nano Res. 15 (2021) 2003–2012.

[28] Q.Z. Huang, Z.J. Tao, L.Q. Ye, H.C. Yao, Z.J. Li, $Mn_{0.2}Cd_{0.8}S$ nanowires modified by CoP_3 nanoparticles for highly efficient photocatalytic H_2 evolution under visible light irradiation, Appl. Catal. B: Environ. 237 (2018) 689–698.

[29] Q.Z. Huang, Y. Xiong, Q. Zhang, H.C. Yao, Z.J. Li, Noble metal-free MoS_2 modified $Mn_{0.25}Cd_{0.75}S$ for highly efficient visible-light driven photocatalytic H_2 evolution, Appl. Catal. B: Environ. 209 (2017) 514–522.

[30] X.W. Jiang, H.S. Gong, Q.W. Liu, M.X. Song, C.J. Huang, In situ construction of $NiSe/Mn_{0.5}Cd_{0.5}S$ composites for enhanced photocatalytic hydrogen production under visible light, Appl. Catal. B: Environ. 268 (2020) 118439.

[31] M.Y. Liu, L.Q. Zhang, X.X. He, B. Zhang, H.F. Song, S.N. Li, W.S. You, L-Cystine-assisted hydrothermal synthesis of $Mn_{1-x}Cd_xS$ solid solutions with hexagonal wurtzite structure for efficient photocatalytic hydrogen evolution under visible light irradiation, J. Mater. Chem. A 2 (2014) 4619.

[32] J.W. Pan, G.X. Zhang, Z.J. Guan, Q.Y. Zhao, G.Q. Li, J.J. Yang, Q.Y. Li, Z.G. Zou, Anchoring Ni single atoms on sulfur-vacancy-enriched $ZnIn_2S_4$ nanosheets for boosting photocatalytic hydrogen evolution, J. Energy Chem. 58 (2021) 408–414.

[33] J. He, L. Chen, F. Wang, Y. Liu, P. Chen, C.T. Au, S.F. Yin, CdS nanowires decorated with ultrathin MoS_2 nanosheets as an efficient photocatalyst for hydrogen evolution, ChemSusChem 9 (2016) 624–630.

[34] S. Ma, Y.P. Deng, J. Xie, K.L. He, W. Liu, X.B. Chen, X. Li, Noble-metal-free Ni_3C cocatalysts decorated CdS nanosheets for high-efficiency visible-light-driven photocatalytic H_2 evolution, Appl. Catal. B: Environ. 227 (2018) 218–228.

[35] J.J. Peng, J. Shen, X.H. Yu, H. Tang, Zulfiqar, Q.Q. Liu, Construction of LSPR-enhanced 0D/2D CdS/MoO_{3-x} S-scheme heterojunctions for visible-light-driven photocatalytic H_2 evolution, Chin. J. Catal. 42 (2017) 87–96.

[36] G.S. Xiao, J.Q. Pan, Y.Y. Fu, Y.Y. Zhang, W.D. Fu, J.J. Niu, J.J. Wang, Y.Y. Zheng, C.R. Li, The $TiO_2/Mn_{0.2}Cd_{0.8}S$ hollow heterojunction with Mn/Cd bimetallic synergy towards photocatalytic hydrogen production enhancement, Int. J. Hydrog. Energy 46 (2021) 28565–28574.

[37] S.W. Du, X. Lin, C.H. Li, G.J. Li, B.B. Zheng, Y. Liu, H. Xu, P.F. Fang, $CoSe_2$ modified Se-decorated CdS nanowire Schottky heterojunctions for highly efficient photocatalytic hydrogen evolution, Chem. Eng. J. 389 (2020) 124431.

[38] W.W. Zhong, S.J. Shen, M. He, D. Wang, Z.P. Wang, Z.P. Lin, W.G. Tu, J.G. Yu, The pulsed laser-induced Schottky junction via in-situ forming Cd clusters on CdS surfaces toward efficient visible light-driven photocatalytic hydrogen evolution, Appl. Catal. B: Environ. 258 (2019) 117967.

[39] Y.X. Wang, C.M. Yang, Y.Y. Zhang, L. Guo, Y. Wang, G. Gao, F. Fu, B. Xu, D. J. Wang, Nanoarchitectonics of $CdS/ZnSnO_3$ heterostructures for Z-Scheme mediated directional transfer of photo-generated charges with enhanced photocatalytic performance, Int. J. Hydrog. Energy 47 (2022) 9566–9578.

[40] C. Li, J.Y. Xue, W. Zhang, F.L. Li, H.W. Gu, P. Braunstein, J.P. Lang, Accelerating water dissociation at carbon supported nanoscale Ni/NiO heterojunction electrocatalysts for high-efficiency alkaline hydrogen evolution, Nano Res. 16 (2023) 4742–4750.

[41] Y.X. Liu, Y.Q. He, C.G. Li, Z. Shi, S.H. Feng, Indium-vacancy-rich $In_2S_3/Ni@C$ photocatalyst with chemical bonds for producing hydrogen and benzylamine oxidation, Sep. Purif. Technol. 324 (2023) 124571.

[42] C.Z. Sun, H. Zhang, H. Liu, X.X. Zheng, W.X. Zou, L. Dong, L. Qi, Enhanced activity of visible-light photocatalytic H_2 evolution of sulfur-doped g-C_3N_4 photocatalyst via nanoparticle metal Ni as cocatalyst, Appl. Catal. B: Environ. 235 (2018) 66–74.

[43] H. Wang, Z.W. Chen, J. Zhang, C.P. Huang, L.Q. Mao, Nickel nanoparticles modified CdS - a potential photocatalyst for hydrogen production through water splitting under visible light irradiation, Int. J. Hydrog. Energy 40 (2015) 340–345.

[44] X.X. Wei, S.H. Xiao, R. Wu, Z.Z. Zhu, L. Zhao, Z. Li, J.J. Wang, J.S. Chen, Z.D. Wei, Activating COOH* intermediate by $Ni/Ni_3ZnC_{0.7}$ heterostructure in porous N-doped carbon nanofibers for boosting CO_2 electroreduction, Appl. Catal. B: Environ. 302 (2022) 120861.

[45] Z.H. Li, Y.F. Yan, S.M. Xu, H. Zhou, M. Xu, L.N. Ma, M.F. Shao, X.G. Kong, B. Wang, L.R. Zheng, H.H. Duan, Alcohols electrooxidation coupled with H_2 production at high current densities promoted by a cooperative catalyst, Nat. Commun. 13 (2022) 147.

[46] L.J. Zhang, R.H. Chen, Y. Tu, X.Y. Gong, X. Cao, Q. Xu, Y. Li, B.J. Ye, Y.F. Ye, J. F. Zhu, Revealing the crystal facet effect of ceria in Pd/CeO_2 catalysts toward the selective oxidation of benzyl alcohol, ACS Catal. 13 (2023) 2202–2213.

[47] R. Du, C.T. Wang, L. Guo, R.A. Soomro, B. Xu, C.M. Yang, F. Fu, D.J. Wang, $NiS/Cd_{0.6}Zn_{0.4}S$ Schottky junction bifunctional photocatalyst for sunlight-driven highly selective catalytic oxidation of vanillyl alcohol towards vanillin coupled with hydrogen evolution reaction, Samll (2023) 2302330.

[48] H.W. Huang, C. Zhou, X.C. Jiao, H.F. Yuan, J.W. Zhao, C.Q. He, J. Hofkens, M.B. J. Roeffaers, J.L. Long, J.A. Steele, Subsurface defect engineering in single-unit-cell Bi_2WO_6 monolayers boosts solar-deiven photocatalytic performance, ACS Catal. 10 (2020) 1439–1443.

[49] C. Yang, Q.Y. Tan, Q. Li, J. Zhou, J.J. Fan, B. Li, J. Sun, K.L. Lv, 2D/2D Ti_3C_2 MXene/g-C_3N_4 nanosheets heterojunction for high efficient CO_2 reduction photocatalyst: dual effects of urea, Appl. Catal. B: Environ. 268 (2020) 118738.

[50] L.D. Li, J.Q. Yan, T. Wang, Z.J. Zhao, J. Zhang, J.L. Gong, N.J. Guan, Sub-10 nm rutile titanium dioxide nanoparticles for efficient visible-light-driven photocatalytic hydrogen production, Nat. Commun. 6 (2015) 5881.

[51] Y.S. Mao, P.F. Wang, S.H. Zhan, Shedding light on the role of interfacial chemical bond in heterojunction photocatalysis, Nano Res. 15 (2022) 10158–10170.

[52] J.Z. Ma, C.X. Wang, H. He, Enhanced photocatalytic oxidation of NO over g-C_3N_4-TiO_2 under UV and visible light, Appl. Catal. B: Environ. 184 (2016) 28–34.

[53] Q. Xi, F.X. Xie, J.X. Liu, X.C. Zhang, J.C. Wang, Y.W. Wang, Y.F. Wang, H.F. Li, Z. B. Yu, Z.J. Sun, X. Jian, X.M. Gao, J. Ren, C.M. Fan, R. Li, In Situ formation $ZnIn_2S_4/Mo_2TiC_2$ Schottky junction for accelerating photocatalytic hydrogen evolution kinetics: Manipulation of local coordination and electronic structure, Samll (2023) 2300717.

[54] J. Wan, L. Liu, Y. Wu, J.R. Song, J.Q. Liu, R. Song, J.X. Low, X.L. Chen, J.J. Wang, F. Fu, Y.J. Xiong, Exploring the polarization photocatalysis of $ZnIn_2S_4$ material toward hydrogen evolution by integrating cascade electric fields with hole transfer vehicle, Adv. Funct. Mater. 35 (2022) 2203252.

[55] H.W. Huang, H.F. Yuan, K.P.F. Janssen, G.S. Fernandez, Y. Wang, C.Y.X. Tan, D. Jonckheere, E. Debroye, J.L. Long, J. Hendrix, J. Hofkens, J.A. Steele, M.B. J. Roeffaers, Efficient and selective photocatalytic oxidation of benzylic alcohols with hybrid organic-inorganic perovskite materials, ACS Energy Lett. 3 (2018) 755–759.

[56] J. Luo, Y.A. Liu, C.Z. Fan, L. Tang, S.J. Yang, M.L. Liu, M.E. Wang, C.Y. Feng, X. L. Ouyang, L.L. Wang, L. Xu, J.J. Wang, M. Yan, Direct attack and indirect transfer mechanisms dominated by reactive oxygen species for photocatalytic H_2O_2 production on g-C_3N_4 possessing nitrogen vacancies, ACS Catal. 11 (2021) 11440–11450.

[57] Z. Wang, T. Inoue, T. Hisatomi, R. Ishikawa, Q. Wang, T. Takata, S.S. Chen, N. Shibata, Y. Ikuhara, K. Domen, Overall water splitting by Ta_3N_5 nanorods single crystals grown on the edges of $KTaO_3$ particles, Nat. Catal. 1 (2018) 756–763.

[58] S.K. Xue, W.Q. Huang, W. Lin, W.D. Xing, M. Shen, X.Y. Ye, X.C. Liang, C. Yang, Y. D. Hou, Z.Y. Yu, X.C. Wang, Interfacial engineering of lattice coherency at ZnO-ZnS photocatalytic heterojunctions, Chem. Catal. 2 (2022) 125–136.

[59] Z. Zhang, J.T.Y.Jr Band, bending in semiconductors: chemical and physical consequences at surfaces and interfaces, Chem. Rev. 112 (2012) 5520–5551.